Simulation of the Flow around Spacer Filaments between Narrow Channel Walls. 1. Hydrodynamics

J. Schwinge,[†] D. E. Wiley,*,[†] and D. F. Fletcher[‡]

UNESCO Centre for Membrane Science and Technology, School of Chemical Engineering and Industrial Chemistry, The University of New South Wales, Sydney, NSW 2052, Australia, and Department of Chemical Engineering, The University of Sydney, Sydney, NSW 2006, Australia

Insights into the effect of spacer filaments in membrane systems on the flow pattern were obtained using a computational fluid dynamics code. The flow patterns were examined for a single filament adjacent to the wall and centered in the channel and for three different spacer configurations, the cavity, zigzag, and submerged spacers, with variations in both the mesh length and filament diameter for Reynolds numbers ranging from 90 to 768. Large recirculation regions were formed behind the filaments, and the flow around the filament increased the shear stress on the wall. For an identical Reynolds number and filament diameter, a single filament adjacent to a membrane wall produced a larger recirculation region than a single filament in the center of the channel. For the cavity and submerged spacers, above a critical Reynolds number or mesh length, the recirculation regions between sequential filaments influenced each other and merged to form one large recirculation region between sequential filaments. In contrast, the zigzag spacer forced the channel flow into a zigzag pattern, which caused the recirculation region to reattach to the wall.

1. Introduction

Water desalination, water reclamation, and product treatment with membrane separation processes are growing applications. Commercial membrane elements for these applications are available in various configurations, of which spiral wound and hollow fiber modules are the most common. The spiral wound module is now the preferred configuration for desalination and water reclamation. Net-type spacers are required in spiral wound modules to keep the membrane leaves apart.

The major problems for the pressure-driven membrane separation processes of reverse osmosis (RO), nanofiltration (NF), ultrafiltration (UF), and microfiltration (MF) are concentration polarization and fouling, which both reduce the flux. Concentration polarization occurs because of the convective transport of solutes to the membrane surface but slower back-diffusion to the bulk. Fouling is a permanent deposition of foulants on the membrane surface, reducing the permeation rate. For a membrane application, the concentration boundary layer must be reduced in order to reduce the wall concentration and fouling. According to boundary layer theory,[1] the higher the velocity, the more the concentration boundary layer thickness at a wall is reduced because of the higher wall shear stress. However, reduction of fouling and concentration polarization by modification of hydrodynamic conditions is limited for spiral wound modules. Spacers, such as those shown in Figure 1, are known to increase the mass transfer because of enhanced wall shear stress and eddy promotion. Therefore, the aim of spacer design is to enhance wall shear stresses and eddy mixing. However, the trade-off for the increased wall shear stress and eddy
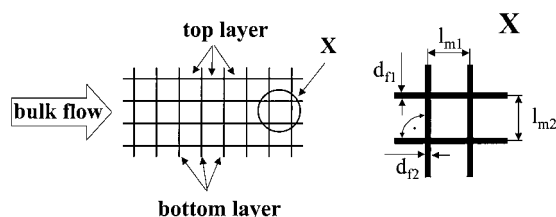

Figure 1. Typical spacer net used in spiral wound modules.

mixing in obstructed channels is the increased pressure loss along the channel.[2–4]

The effect of spacer configurations on pressure loss and mass transfer was investigated experimentally in cross-flow test cells.[2–10] Flux enhancements of 3 times and more have been reported for spacer-filled channels when compared with empty channels.[2–7] The pressure loss measurements in a spacer-filled channel showed a complex dependence on filament diameter, mesh length, channel height, the angle between the filaments, and the angle of the spacer filaments toward the main flow direction. The spacer filaments increase the pressure loss because of a large increase of the viscous and form drag. Belfort and Guter[8] evaluated the mass-transfer and pressure loss characteristics of various spacer nets for electrodialysis, and their pressure loss measurements indicated that spacers induce turbulent flow characteristics.

Kozlu et al.[11] examined the enhancement of heat transfer in a rectangular channel by microgrooves on the wall and microcylinders placed near the channel wall for Reynolds numbers up to 100 000. They found that the microcylinders effectively enhance the heat transfer, but the optimum performance showed a dependence on the Reynolds number and microcylinder position.

Many researchers have examined flow around cylinders placed in the middle of a wide channel where interactions with the channel walls are neglected. For

---

* Corresponding author. Tel.: + 61 2 9385 4304. Fax: + 61 2 9385 5966. E-mail: D.Wiley@unsw.edu.au.
† The University of New South Wales.
‡ The University of Sydney.

this type of flow around "free" cylinders, the numerical analyses focused on the area near the cylinder surface. It was found that no eddy existed behind the cylinder for a Reynolds number of 0.01. For Reynolds numbers above 40, the recirculation region started to show periodic movements and the flow became unsteady. For a Reynolds number greater than 200, the flow was found to be unsteady with a large eddy formed behind the cylinder. However, the flow in obstructed channels becomes unsteady at much smaller Reynolds numbers than that for the flow in an empty channel. The flow can become unsteady and show periodic movements for Reynolds numbers as low as 200 depending on the geometry of the obstruction and is unsteady for Reynolds numbers above 600.[12-16] Greiner et al.[17-19] examined the heat-transfer enhancement by grooved channels. They confirmed that the flow became unsteady above a critical Reynolds number of about 600. The pressure gradients were roughly equal for the grooved and flat channels for subcritical Reynolds numbers but increased significantly for the grooved channel for supercritical Reynolds numbers. Majumdar and Amon[20] and Amon et al.[21] examined unsteady flows caused by rectangular bars located in the center of the channel. They also found that for multiple rectangular bars the flow started to become unsteady for a Reynolds number above 200.

The flow profiles in front of and behind rectangular bars and filaments attached to a wall have also been investigated.[22-24] Kang and Chang[24] showed experimentally and numerically that a large eddy region was found to exist behind a filament and a smaller eddy region was formed in front of a filament. The eddy region and the reattachment zone were shown to cause mass-transfer enhancement. The size of the eddies increased with the Reynolds number.

An initial attempt at using a computational fluid dynamics (CFD) package to model two-dimensional fluid flow around cylindrical spacer filaments in narrow channels was undertaken by Cao et al.[25] Cao et al. confirmed that eddy formation occurred before and after the cylindrical spacer filaments in narrow channels. Configurations examined had the filaments either adjacent to a wall or located in the center of the channel.

The experimental and numerical investigations of spacer-filled channels have revealed the importance of the hydrodynamics on mass-transfer and pressure loss enhancement along a channel in a spiral wound module. Further optimization of spacer designs requires detailed knowledge of the complex dependencies of the filament diameter, mesh length, and filament configurations on the fluid flow. With the development of CFD packages, the simulation and visualization of flows around multiple filaments in a channel have become possible. This paper investigates the effects of single and multiple filaments in narrow channels on the flow patterns.

2. Numerical Method and Modeling Assumptions

In smooth empty channels, the flow is laminar for Reynolds numbers up to 2000.[1] However, the flow in narrow obstructed channels becomes unsteady at much smaller Reynolds numbers.[11-21] In this paper, flow in a narrow spacer-filled channel is modeled for Reynolds numbers between 90 and 768. The effect of the filament geometry on the flow patterns is examined extensively for lower Reynolds numbers, which do not cause any
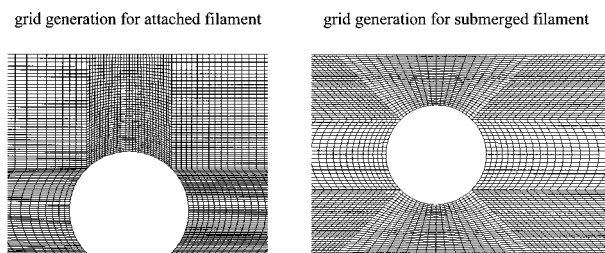

Figure 2. Section of the grid generated around a transverse filament either adjacent to a wall or submerged in the center of the channel.

large-scale vortex shedding. The fluid used is water at a temperature of 293 K. It is assumed to be incompressible and isothermal and to have constant fluid properties. The fluid motion is described by the Navier–Stokes equations. The governing Navier–Stokes equations are valid for all Reynolds numbers, but under laminar conditions, they can be solved without the need to consider the resolution of turbulent eddies.[26,27]

These equations were solved using a CFD code (CFX4, Version 4.3; AEA Technology). The software uses a finite volume method on a co-located grid to solve the conservation equations. The pressure–velocity coupling is handled via the SIMPLEC algorithm, and the QUICK differencing scheme was used throughout the simulations.[27] In this paper, simulations were restricted to flows without any large-scale vortex shedding behind the filaments. For lower Reynolds numbers, the fluid flow was steady and convergence was achieved in less than 1500 iterations. For larger Reynolds numbers, the flow became transient. However, even for the larger Reynolds numbers and smaller filament diameters simulated here, the flow did not show any large-scale vortex shedding and convergence was achieved in the transient mode within a maximum of 40 iterations at each time step, with relaxation factors of 0.7–0.9. The sum of the mass residuals was less than 0.01% of the inlet flux, ensuring a high degree of convergence. For multiple filament configurations, the whole computational domain was used.

A small enough grid size was chosen, based on the comparison of results from a succession of finer meshes, to ensure that the results were independent of the grid. An example of the grid generated around a filament adjacent to a wall and submerged in the center of the channel is shown in Figure 2. Each cylindrical filament attached to the wall was divided into three sections with an angular resolution of 90° covering −45° to +225°. The grid generated for the filament depended on the filament diameter. The top part of the filament had more than 25 mesh points, and both sides each had more than 40 mesh points. For the filaments submerged in the center of the channel, the cylindrical filament was divided into four 90° sections. Both sections facing sideways were resolved using more than 40 mesh points, and the two sections facing the walls were split into more than 25 mesh points. The entrance length was meshed using a one-way bias over 50 mesh points, with the points next to the filaments being 15 times closer together than those at the channel entrance. Similarly, the channel exit mesh was one-way-biased over 80 grid points, with the grid points next to the filaments being 15 times closer together than those at the channel exit. The part of the channel between the top of the filament and the opposite wall had more than 25 grid points. The number of cells generated depended on the number of
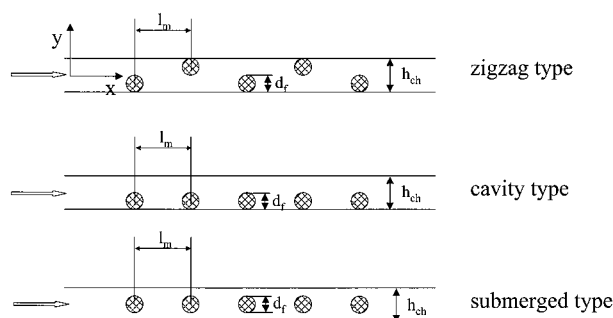
Figure 3. Transverse filament configurations used in the channel to obstruct the flow.

filaments used for the simulation run. For example, for a single transverse filament ($d_f/h_{ch} = 0.5$), more than 22 000 elements were generated for the channel, as shown in Figure 2.

3. Problem Description

3.1. Channel Geometry. Commercially, spacer nets are produced with various mesh lengths, filament diameters, and channel heights leading to complex geometries. However, for a fundamental understanding of flows in narrow channels with cylindrical obstructions, this paper focuses on cylindrical spacer filaments that were orientated transverse to the main flow direction. Using filaments located transverse to the main flow direction permitted two-dimensional CFD simulations for all calculations. These two-dimensional calculations are an excellent screening and benchmarking device for future evaluations of more complex spacer geometries and allow the effect of numerical parameters and modeling assumptions to be studied for situations in which grid independence can be guaranteed. Figure 3 shows the three different spacer configurations that were examined: (a) the filaments were placed alternately adjacent to the top and bottom walls (zigzag type), (b) all of the filaments were placed adjacent to only one wall (cavity type), and (c) the filaments were located in the center of the channel (submerged type). The channel contained multiple filaments to demonstrate the repetition of the flow profile and the filament−filament interactions between sequential filaments.

The entrance length of the channel was at least 10 times the filament diameter, while the exit length was at least twice the entrance length to avoid any effects of the channel exit on eddy formation behind the filaments. In all cases, the inlet velocity was specified as normal to the channel entrance and the flow was fully developed before reaching the first upstream filament. For the exit of the channel, a constant pressure was defined. Because this paper focuses on the fluid flow patterns around and between sequential filaments, as a first approximation, the wall was assumed to be nonpermeable because permeate recoveries are usually low for membrane applications.[25]

The spacer-filled channel is characterized by the filament diameter d_f, the mesh length l_m, the channel height h_{ch}, the channel Reynolds number Re_{ch}, and the following dimensionless groups: the dimensionless filament diameter (filament diameter to channel height ratio) d_f/h_{ch}, the dimensionless mesh length (mesh length to channel height ratio) l_m/h_{ch}, and the Reynolds number Re_{ch}. The present simulations cover the ranges

(i) $d_f/h_{ch} = 0.16-0.7$, (ii) $l_m/h_{ch} = 1-12$ with only d_f/h_{ch} as a characterization for a single filament, and (iii) $Re_{ch} = 90-768$. For multiple filaments, the mesh length to filament diameter ratio l_m/d_f is another dimensionless group, which can be substituted for either d_f/h_{ch} or l_m/h_{ch}. Here, the l_m/d_f ratio covers the range (iv) $l_m/d_f = 1.4-75$. The channel Reynolds number is defined as

$$Re_{ch} = d_h u_{ave}/\nu \tag{1}$$

where d_h is the hydraulic diameter for a spacer-filled flow channel:[28]

$$d_h = \frac{4\epsilon}{\dfrac{2}{h_{ch}} + (1 - \epsilon)S_{VSP}} \tag{2}$$

where S_{VSP} is the specific surface area of the spacer filament in the channel:

$$S_{VSP} = \frac{S_{SP}}{V_{SP}} = \frac{4}{d_f} \tag{3}$$

and where ϵ is the voidage of the spacer-filled channel:

$$\epsilon = \frac{V_{tot} - V_{SP}}{V_{tot}} \tag{4}$$

In contrast to the Reynolds number for the spacer-filled channel Re_{ch}, the Reynolds number for flow around a cylindrical filament Re_{cyl} placed in a flowing stream where the walls are infinitely far away is defined as

$$Re_{cyl} = d_f u/\nu \tag{5}$$

When a spacer filament is adjacent to a wall, a recirculation region of length L_R is formed behind the filament, where the reattachment length is defined by the point where the separation streamline reattaches to the wall.[24] Fletcher et al.[29] successfully used a power law to relate the reattachment length to the Reynolds number and the geometry of a sudden expansion. From dimensional analysis, a similar power law can be used here for a single filament in the channel. The length of the recirculation region L_R can be written in terms of dimensionless groups as follows:

$$\frac{L_R}{h_{ch}} = \lambda Re_{ch}{}^{\beta}\left(\frac{d_f}{h_{ch}}\right)^{\gamma} \tag{6}$$

To study the effects of the velocity and filament diameter on the flow pattern, a single filament was used. Additionally, to study the effects of the mesh length on the flow pattern and pressure loss, multiple filaments were used in the channel. The pressure loss along the spacer-filled channel was used to determine the total drag coefficient C_{TD} and friction factor for the filament configurations according to[2,3]

$$C_{TD} = 4f = 2\Delta p_{ch} d_h/\rho u^2 L \tag{7}$$

3.2. Evaluation of the Calculated Results. The quality of the simulated results obtained in this paper was evaluated by a comparison with results published by Kang and Chang.[24] Kang and Chang conducted experimental and numerical analysis of flow patterns in a rectangular channel with transverse rectangular

bars obstructing the flow. For the comparison, the same channel dimensions and Reynolds numbers (50−400) of Kang and Chang were used. The CFX results showed excellent agreement with the data published by Kang and Chang. For example, at a Reynolds number of 100, an identical formation of the recirculation regions before and after the rectangular bar was found. The length of the recirculation region and the location of the reattachment zone were also identical. At a Reynolds number of 200, both the CFX simulation and the data from Kang and Chang predicted the recirculation region detaching from the wall. The eddy behind the first rectangular bar and in front of the downstream rectangular bar formed a region between the filaments where the two eddies merged to form a large recirculation zone.

4. Flow Patterns in Narrow Channels with a Single Filament Transverse to the Flow

4.1. Examination of the Stability of the Recirculation Regions behind Filaments in Narrow Channels. The stability of the eddy region was checked for channel Reynolds numbers between 90 and 768. In the transient mode of CFX, time steps of 30 μs were used and convergence was achieved with a maximum of 40 iterations for each step. Monitoring points in the recirculation region showed no fluctuations of pressure or velocity, and thus no evidence of transient flow was found, despite using small time steps and a fine mesh, for small Reynolds numbers. With an increase in the filament diameter and Reynolds numbers, the recirculation region started to show periodic movements, and for a further increase in the Reynolds number, vortex shedding occurred. For the smallest filament diameter d_f/h_{ch} equal to 0.16, the Reynolds number was increased to higher values to determine when the flow becomes unsteady. For the highest channel Reynolds number, $Re_{ch} = 768$ and $Re_{cyl} = 61$ with the filament adjacent to the wall, no vortex shedding was found. However, for the filament located in the center of the narrow channel, transient flows occurs at smaller Reynolds numbers than those for filaments adjacent to the wall.

For a cylinder in a "free-flow" channel, the flow starts to become transient for Re_{cyl} above 40, and for Re_{cyl} greater than 200, the flow is fully transient with vortex shedding.[26,30] Therefore, in the case of a narrow channel, it is clear that the walls damp the transition. In addition, because the calculations were completed for a two-dimensional channel, any effects causing instability in a three-dimensional flow are not present. All subsequent results reported in this paper are for Reynolds numbers below those at which large-scale vortex shedding occurs.

4.2. Flow Profile around a Single Filament Adjacent to a Wall. Computations were carried out for a single filament adjacent to the bottom wall of the flow channel for Reynolds numbers Re_{ch} varying from 90 to 768 with dimensionless filament diameters of 0.16, 0.35, 0.5, and 0.7, while the larger Reynolds numbers were only used for the smallest filament diameter. Figure 4 shows a part of the flow channel with the filament and the recirculation region before and after the filament.

A very small recirculation region is formed in front of the filament and a much larger recirculation region is formed behind the filament, and the local velocity increases between the filament and the wall because of
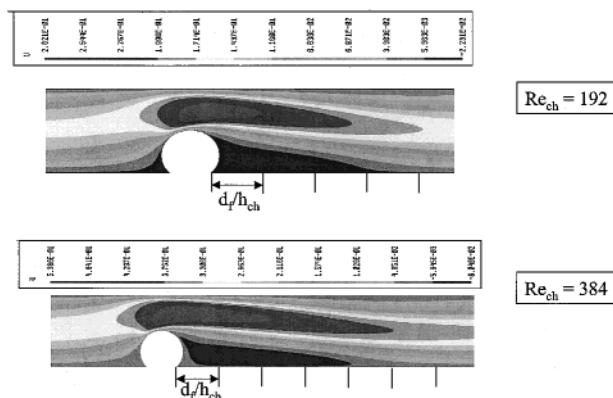
Figure 4. Flow around a single filament adjacent to the bottom wall for Re_{ch} of 192 and 384 ($d_f/h_{ch} = 0.5$).
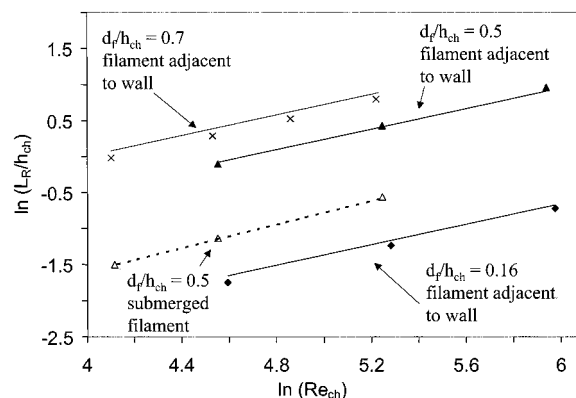
Figure 5. Dependence of the dimensionless reattachment length L_R/h_{ch} on Reynolds number Re_{ch} for d_f/h_{ch} of 0.16, 0.5, and 0.7.

the flow around the filament. The maximum velocity in that region is found to be 2.7 times the inlet velocity. The high velocity between the top of the filament and the opposite wall leads to a high shear stress region at the wall. The shear stress on the wall increases with the filament diameter and Reynolds number.

For $Re_{ch} = 384$ and $d_f/h_{ch} = 0.5$, the shear stress is increased by up to 10 times above the filament at the top wall when compared with the empty channel. At the bottom wall, within the recirculation region behind the filament, the shear stress is increased by up to a factor of 2. For a larger filament diameter of $d_f/h_{ch} = 0.7$, the wall shear stress increases locally by up to 28 times on the wall opposite the filament when compared with the empty channel, and a filament diameter of $d_f/h_{ch} = 0.7$ has an up to 6 times larger shear stress enhancement when compared with the filament diameter of $d_f/h_{ch} = 0.16$.

As shown in Figures 5 and 6, the length of the steady recirculation region L_R/h_{ch} increases with Re_{ch} and filament diameter d_f/h_{ch}. The figures show the calculated points, and the lines drawn show the fit by a multilinear regression. For a constant filament diameter as shown in Figure 5, the following correlations between L_R/h_{ch} and Re_{ch} are obtained:

$$L_R/h_{ch} \propto Re_{ch}^{0.74} \qquad \text{for } d_f/h_{ch} = 0.16 \qquad (8a)$$

$$L_R/h_{ch} \propto Re_{ch}^{0.77} \qquad \text{for } d_f/h_{ch} = 0.5 \qquad (8b)$$

$$L_R/h_{ch} \propto Re_{ch}^{0.79} \qquad \text{for } d_f/h_{ch} = 0.7 \qquad (8c)$$
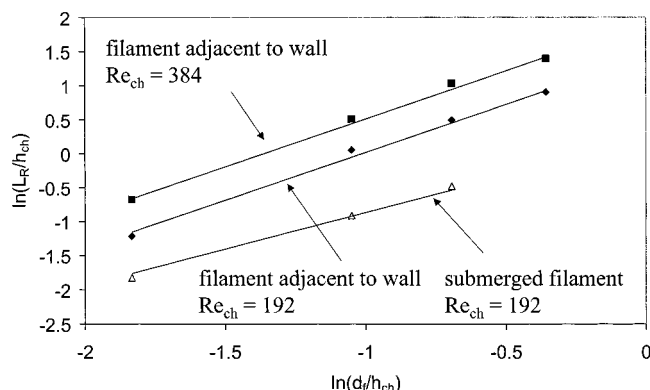
Figure 6. Dependence of the dimensionless reattachment length L_R/h_{ch} on dimensionless filament diameter d_f/h_{ch} for Re_{ch} of 192 and 384.

For a constant Re_{ch} as shown in Figure 6, the following correlations are obtained:

$$\frac{L_R}{h_{ch}} \propto \left(\frac{d_f}{h_{ch}}\right)^{1.47} \qquad \text{for } Re_{ch} = 192 \qquad (9a)$$

$$\frac{L_R}{h_{ch}} \propto \left(\frac{d_f}{h_{ch}}\right)^{1.52} \qquad \text{for } Re_{ch} = 384 \qquad (9b)$$

Equations 8a–9b indicate that the length of the recirculation region increases with both Re_{ch} and d_f/h_{ch}. The recirculation region also develops more rapidly at higher Re_{ch} and d_f/h_{ch}, as can be seen from the slight increase of the exponents in each set. A multilinear regression resulted in the following equation for predicting the length of the steady recirculation region L_R/h_{ch}:

$$\frac{L_R}{h_{ch}} = 0.097 Re_{ch}^{0.71} \left(\frac{d_f}{h_{ch}}\right)^{1.41} \qquad (10)$$

4.3. Flow Profile around a Single Filament Submerged in the Center of the Channel. Simulations were carried out for a single filament located in the center of the channel with dimensionless filament diameter ratios d_f/h_{ch} of 0.16, 0.35, 0.5, and 0.7. The simulations were conducted for $Re_{ch} = 90$–768, with the larger Reynolds numbers being used only for the smallest filament diameter. A recirculation region is formed behind the filament, as shown in Figure 7. The length of the recirculation region increases with the Reynolds number and filament diameter. When Re_{ch} is increased to 400 ($d_f/h_{ch} = 0.5$ and $Re_{cyl} = 100$), the recirculation is unsteady and shows periodic movements. For the steady recirculation regions behind the filament, the following relationships are obtained for the length of the recirculation region:

$$\frac{L_R}{h_{ch}} \propto Re_{ch}^{0.84} \qquad \text{for } d_f/h_{ch} = 0.5 \qquad (11a)$$

$$\frac{L_R}{h_{ch}} \propto \left(\frac{d_f}{h_{ch}}\right)^{1.22} \qquad \text{for } Re_{ch} = 192 \qquad (11b)$$

In comparison with a filament adjacent to the wall, the submerged filament has a shorter recirculation region behind the filament, which highlights the effect of the interaction between the wall and the filament adjacent to it on the formation of the recirculation
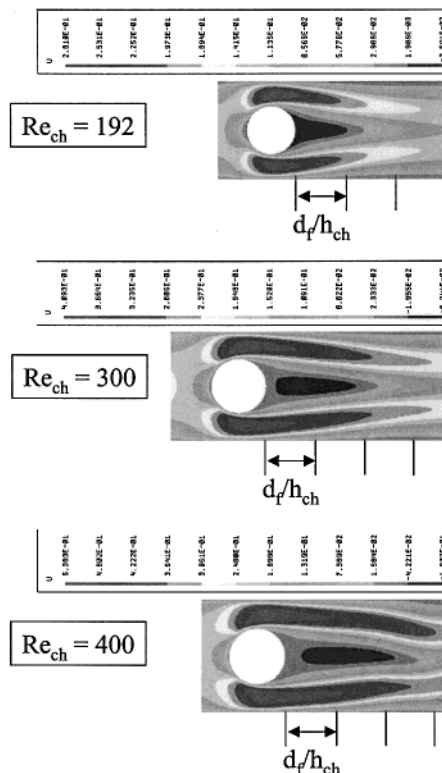
Figure 7. Flow around a single filament submerged in the center of the channel for Re_{ch} of 192, 300, and 400 ($d_f/h_{ch} = 0.5$).

region. However, at an identical dimensionless filament diameter d_f/h_{ch}, the exponent of Re_{ch} for a submerged filament is 10% larger, which means that the steady recirculation region behind a submerged filament grows more rapidly with Re_{ch}.

A multilinear regression on L_R/h_{ch}, Re_{ch}, and d_f/h_{ch} correlates the length of the steady recirculation region behind the submerged filament as follows:

$$\frac{L_R}{h_{ch}} = 0.016 Re_{ch}^{0.82} \left(\frac{d_f}{h_{ch}}\right)^{1.08} \qquad (12)$$

The regression equations in eqs 8, 9, and 11 are in good agreement with the calculated data points within a maximum error of 5%. Equations 10 and 12 achieve good agreement with the calculated results for the entire range of Reynolds numbers and filament diameters. For filament diameters of d_f/h_{ch} equal to 0.5 and below, the predictions have a maximum error of 10%. However, for the larger filament diameter of d_f/h_{ch} equal to 0.7, eqs 10 and 12 overpredict the length of the recirculation regions by more than 10%.

The submerged filament has a similar maximum velocity between the filament and the wall when compared with a filament adjacent to the wall. However, the maximum wall shear stress directly above and below the filament is locally much higher, as shown in Table 1.

5. Flow Patterns in Narrow Channels with Multiple Filaments Transverse to the Flow

The flow patterns for multiple filaments were examined for the three filament configurations depicted in Figure 3: the zigzag, the cavity, and the submerged spacers, respectively. Figures 8–10 show truncated flow

Table 1. Values for the Shear Stress on Both the Top and Bottom Walls for the Flow around a Single Filament Either Adjacent to the Bottom Wall or Submerged in the Center of the Channel at $d_f/h_{ch} = 0.5$

Re_{ch}	filament location	max absolute value of the wall shear stress on the bottom wall [N/m²]	max absolute value of the wall shear stress on the top wall [N/m²]
192	adjacent	0.5	3.4
192	submerged	5.7	5.7
384	adjacent	1.4	8.8
384	submerged	13.5	13.5
684	adjacent	4.4	22.1

patterns for two to five sequential filaments from simulations of the whole computational domain.

5.1. Flow Profile around Multiple Filaments Adjacent to the Bottom Wall. For the studies of the effects of the multifilament cavity spacer on the flow patterns between sequential filaments, the dimensionless mesh length l_m/h_{ch} ranged from 1 to 12 with dimensionless filament diameters d_f/h_{ch} of 0.16, 0.3, 0.5, and 0.7 and Re_{ch} ranged from 90 to 684, again with the larger Reynolds numbers being used only for the smallest filament diameter.

Studies of the effect of Re_{ch} on the flow pattern, as shown in Figure 8a, demonstrate that the multifilament cavity spacer at a mesh length of $l_m/h_{ch} = 4$ has separate recirculation regions before and after each filament for Re_{ch} below 171, just as was observed for a single filament. For Re_{ch} of 171, the recirculation regions start to merge to form a single but highly asymmetric recirculation region, and a further increase of Re_{ch} above 171 produces one large "fully formed" recirculation region between sequential filaments. For Re_{ch} below 90, the high-velocity region between the filament and the wall is located above the filament and had little effect on the flow around the next filament. As Re_{ch} is increased above 90, the tail of the high-velocity region extends further downstream until it meets and merges with the high-velocity region of the downstream filament.

For studies of the effect of the mesh length on the flow pattern at a mesh length l_m/h_{ch} above 6 ($Re_{ch} = 148$ and $d_f/h_{ch} = 0.5$), separate recirculation regions were formed between sequential filaments. When l_m/h_{ch} was decreased below 6, the separation streamline detaches from the wall. For l_m/h_{ch} of 3 and below, one large recirculation region is formed between sequential filaments, as shown in Figure 8b.

Figure 8c shows the flow pattern for d_f/h_{ch} between 0.16 and 0.7 ($Re_{ch} = 162$ and $l_m/h_{ch} = 4$). For $d_f/h_{ch} = 0.16$ and 0.35, separate recirculation regions were formed between sequential filaments, while for $d_f/h_{ch} = 0.7$, one large recirculation region is formed between sequential filaments. The maximum velocity between the top of the filament and the opposite wall is 1.6 times the inlet velocity for $d_f/h_{ch} = 0.16$, 2 times the inlet velocity for $d_f/h_{ch} = 0.35$, and 4 times the inlet velocity for $d_f/h_{ch} = 0.7$.

For the range of d_f/h_{ch} from 0.16 to 0.7 examined here, the separation streamline detaches from the wall when the characteristic mesh length to filament diameter ratio l_m/d_f is decreased below 8 at $Re_{ch} = 162$. The characteristic value of l_m/d_f indicates that the change in the flow pattern between sequential filaments increases with Re_{ch}.

The characteristic shear stress distribution for the cavity spacer with the filaments adjacent to the bottom wall is shown in parts d and e of Figure 8. For $l_m/h_{ch} = 4$ with a "fully formed" recirculation region between sequential filaments, an enhanced shear stress region is caused by the reverse flow in the recirculation region behind each filament on the bottom wall. For $l_m/h_{ch} = 8$ with two separate recirculation regions between sequential filaments, the shear stress is enhanced within each recirculation region on the bottom wall, as shown in Figure 8d. For both dimensionless mesh lengths l_m/h_{ch} of 4 and 8, the maximum absolute wall shear stress on the top wall is achieved immediately above each filament and the lowest wall shear stress was achieved halfway between the filaments, as shown in Figure 8e.

5.2. Flow Profile around Multiple Filaments Alternately Adjacent to the Top and Bottom Walls. For the studies of the effects of the multifilament zigzag spacer on the flow pattern between sequential filaments, the dimensionless mesh length l_m/h_{ch} ranged from 1 to 12 with dimensionless filament diameters d_f/h_{ch} of 0.16, 0.3, 0.5, and 0.7 and Re_{ch} ranged from 90 to 684, again with the larger Reynolds numbers being used only for the smallest filament diameter.

Figure 9a shows the effect of Re_{ch} on the flow pattern for the multifilament zigzag spacer at $l_m/h_{ch} = 3$. The main flow stream passes the upstream filament and then is forced to change direction because of the presence of the sequential downstream filament at the opposite wall. Similar to a single filament adjacent to the wall, a small recirculation region is formed before each filament and another much larger one is formed behind each filament. The size and length of the recirculation region L_R/h_{ch} increased with Re_{ch}. However, when Re_{ch} is increased above 148 at $l_m/h_{ch} = 3$, the size and length of the recirculation regions does not increase further because the zigzag geometry forces the recirculation region to reattach to the wall and restricts any further enlargement of the recirculation regions. As the flow is forced around the filaments, a maximum velocity is observed between the top of each filament and the opposite wall that is 2.7 times the inlet velocity, which is similar to the enhancement for multiple filaments adjacent to the bottom wall.

The effect of the mesh length on the zigzag flow pattern at fixed values of $Re_{ch} = 171$ and $d_f/h_{ch} = 0.5$ is shown in Figure 9b. At small Re_{ch} or large mesh lengths, the size and length of the recirculation region varies in the same manner as that for a single filament adjacent to the wall. As the mesh length decreases, the flow is forced to zigzag around the filaments, with the size and length of the recirculation region being restricted by the mesh length, as shown in Figure 9c.

For the zigzag spacer, the recirculation region reattaches to the wall even for smaller mesh lengths. Only when the mesh length is reduced to values of l_m/h_{ch} below unity does the separation streamline detach from the wall and is a "fully formed" recirculation region formed between sequential filaments. However, such a small mesh length is impractical for spacers in spiral wound modules.

The effect of the filament diameter on the flow pattern is shown in Figure 9d. At $d_f/h_{ch} = 0.7$ ($l_m/h_{ch} = 4$ and $Re_{ch} = 167$), there is a strong zigzag pattern enforced on the flow along the channel. For $d_f/h_{ch} = 0.2$ ($l_m/h_{ch} = 4$ and $Re_{ch} = 167$), the small filament diameter does not force the flow into a strong zigzag pattern because the
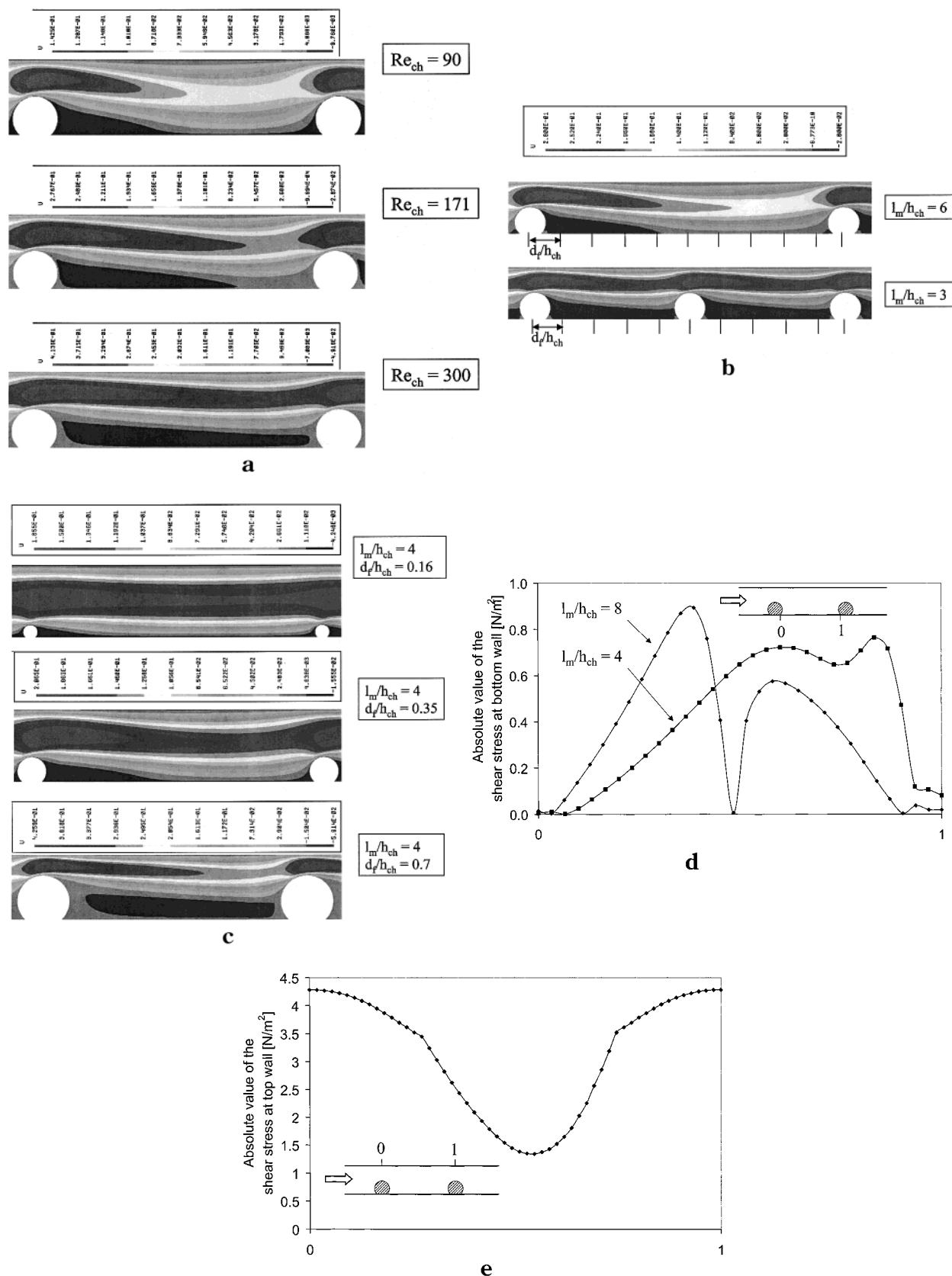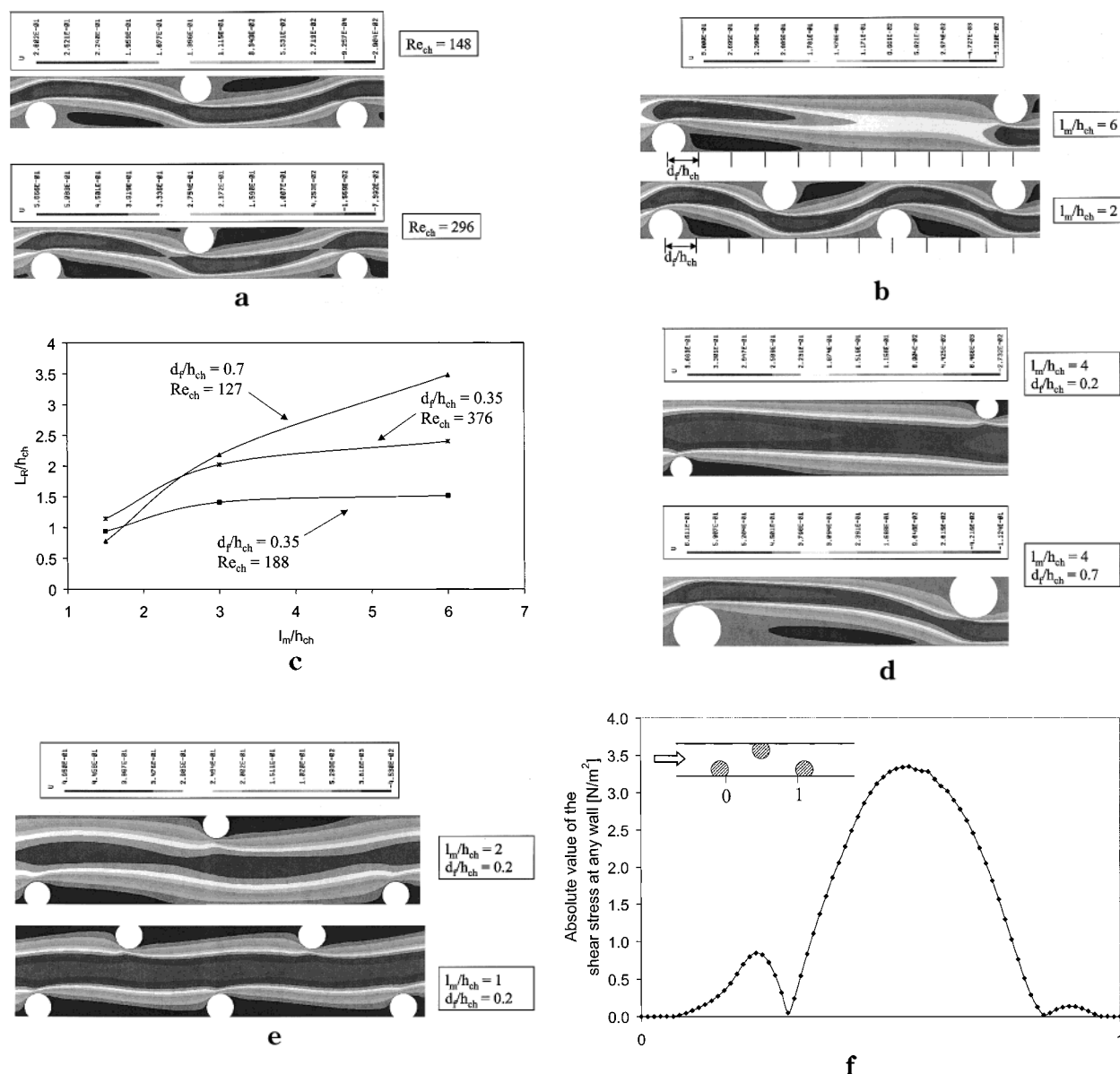
Figure 8. (a) Flow between sequential filaments for the cavity spacer for Re_{ch} of 90, 171, and 300 ($l_m/h_{ch} = 4$ and $d_f/h_{ch} = 0.5$). (b) Flow between sequential filaments for the cavity spacer showing the effect of mesh length ($l_m/h_{ch} = 6$ and 3, $Re_{ch} = 148$, and $d_f/h_{ch} = 0.5$). (c) Flow between sequential filaments for the cavity spacer showing the effects of the filament diameter (l_m/h_{ch} equal to 0.16, 0.35, and 0.7, $Re_{ch} = 162$, and $l_m/h_{ch} = 4$). (d) Shear stress distribution for the cavity spacer on the bottom wall between sequential filaments ($d_f/h_{ch} = 0.5$, $l_m/h_{ch} = 4$ and 8, and $Re_{ch} = 300$). (e) Shear stress distribution for the cavity spacer on the top wall between sequential filaments ($d_f/h_{ch} = 0.5$, $l_m/h_{ch} = 4$ and 8, and $Re_{ch} = 300$).

filament on one wall hardly influences the fluid flow on the opposite wall. When the mesh length is decreased

for $d_f/h_{ch} = 0.2$, the flow pattern between sequential filaments becomes similar to the flow pattern for the

Figure 9. (a) Flow between sequential filaments for the zigzag spacer for Re_{ch} of 148 and 296 ($l_m/h_{ch} = 3$ and $d_f/h_{ch} = 0.5$). (b) Flow between sequential filaments in a zigzag configuration showing the effect of mesh length ($l_m/h_{ch} = 6$ and 2, $Re_{ch} = 171$, and $d_f/h_{ch} = 0.5$). (c) Reattachment length L_R/h_{ch} for the zigzag spacer as a function of mesh lengths l_m/h_{ch} (d_f/h_{ch} equal to 0.35 and 0.7 and Re_{ch} from 127 to 376). (d) Flow pattern for the zigzag spacer at filament diameters of d_f/h_{ch} equal to 0.2 and 0.7 ($Re_{ch} = 167$ and $l_m/h_{ch} = 4$). (e) Flow pattern for the zigzag spacer with $d_f/h_{ch} = 0.2$ at $Re_{ch} = 376$ for l_m/h_{ch} equal to 1 and 2. (f) Shear stress distribution for the zigzag spacer on the top wall between sequential filaments ($d_f/h_{ch} = 0.5$, $l_m/h_{ch} = 4$, and $Re_{ch} = 171$).

cavity spacer. One large recirculation region is formed between sequential filaments on the same wall, and the main flow passes through the center of the channel, as shown in Figure 9e.
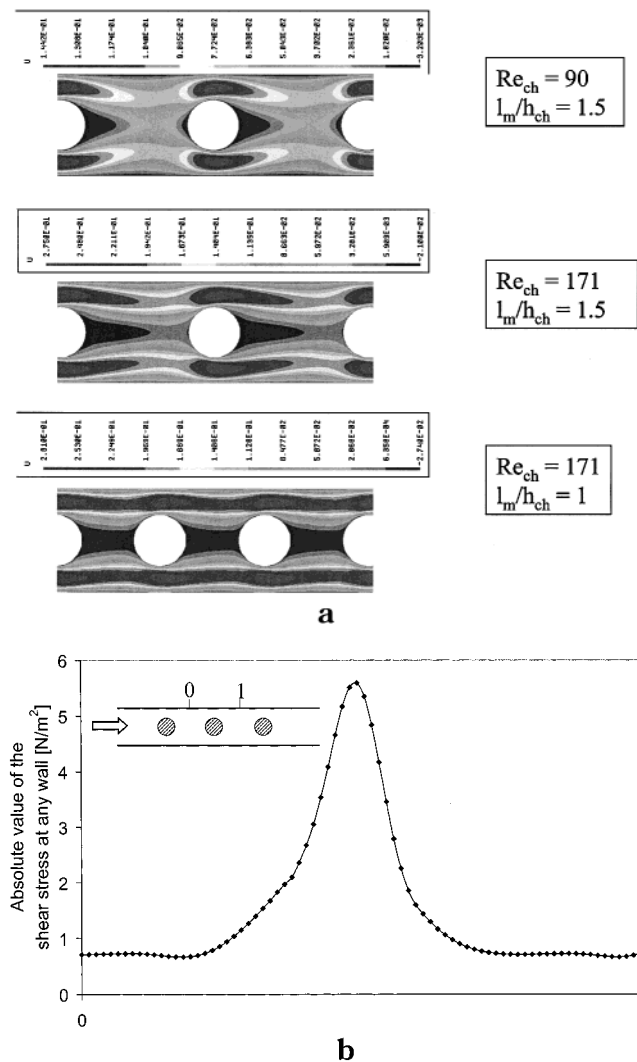
The characteristic shear stress distribution, as shown in Figure 9f, has three local maxima of the absolute shear stress values between sequential filaments. The highest wall shear stress occurs at the wall immediately above and opposite each filament. Smaller local maxima of the absolute shear stress value occur in front of and behind each filament because of the recirculation regions.

5.3. Flow Profile around Multiple Filaments Submerged in the Center of the Channel. For the studies of the effects of the multifilament submerged spacer on the flow pattern between sequential filaments, the dimensionless mesh length l_m/h_{ch} ranged from 1 to 12 with dimensionless filament diameters d_f/h_{ch} of 0.16,

0.3, 0.5, and 0.7 and Re_{ch} ranged from 90 to 684, while the larger Reynolds numbers were only used for the smallest filament diameter to avoid any large-scale vortex shedding.

For studies of the effect of Re_{ch} at a mesh length of $l_m/h_{ch} = 1.5$ and a dimensionless filament diameter $d_f/h_{ch} = 0.5$, the flow pattern of the multifilament submerged spacer is shown in Figure 10a. A recirculation region is produced behind each filament in the center of the channel just as for a single submerged filament. At Re_{ch} equal to 171, the formation of the recirculation region between sequential filaments is influenced by the downstream filament and starts to form one large "fully formed" recirculation region. When the mesh length is decreased at the identical Re_{ch}, one "fully formed" large recirculation region is formed between sequential filaments. When compared with the cavity spacer, the submerged spacer forms "fully formed" recirculation

Figure 11. Pressure loss along the channel for the three filament configurations at different mesh lengths ($d_f/h_{ch} = 0.5$ and $Re_{ch} = 177$) and at different filament diameters ($l_m/h_{ch} = 6$ and $Re_{ch} = 342$).

the mesh length decreased at fixed Re_{ch}, the separate recirculation regions merge to form one large recirculation region between sequential filaments. For the submerged spacer, l_m/h_{ch} must be reduced to smaller values or Re_{ch} must be increased to larger values to obtain one large recirculation region between sequential filaments when compared with the cavity spacer. This is due to the fact that the recirculation region is larger for filaments adjacent to the wall, which favors an interaction of the recirculation regions between sequential filaments at larger values of l_m/h_{ch}.

6. Pressure Loss for the Flow around the Spacer Filaments

The obstruction of the flow channel by the spacer filaments increases the pressure loss due to the additional form drag caused by each spacer filament. For all multifilament configurations, the pressure loss increases with the Reynolds number and filament diameter and decreases in mesh length. Figure 11 shows that the pressure loss increases as the mesh length decreases, with the submerged spacer having the highest pressure loss at fixed Re_{ch} and d_f/h_{ch}. For $l_m/h_{ch} > 4$ ($d_f/h_{ch} = 0.5$ and $Re_{ch} = 177$), the zigzag spacer has a pressure loss similar to that of the cavity spacer. For $l_m/h_{ch} < 4$, the pressure loss of the zigzag spacer becomes larger than that of the cavity spacer because of the large drag produced when the flow is forced into the zigzag flow pattern.

Figure 11 also shows that the pressure loss increases with the filament diameter, with the submerged spacer again having the highest pressure loss. The zigzag spacer shows a similar pressure loss when compared with the cavity spacer at a fixed mesh length $l_m/h_{ch} = 6$ and small filament diameters. As the filament diameter increases, the pressure loss of the zigzag spacer increases more rapidly than that of the cavity spacer because of the enforced zigzag streaming of the flow.

The friction factor is depicted in Figure 12 for mesh lengths ranging from 3 to 12 and for the empty channel. The friction factor is significantly higher for all spacers when compared with the empty channel even at the low Reynolds numbers used here. The friction factor is roughly similar for the zigzag and cavity spacers but is higher for the submerged spacer. The friction factor of the submerged spacer is found to be the highest because of the flow around both sides of the filaments and the
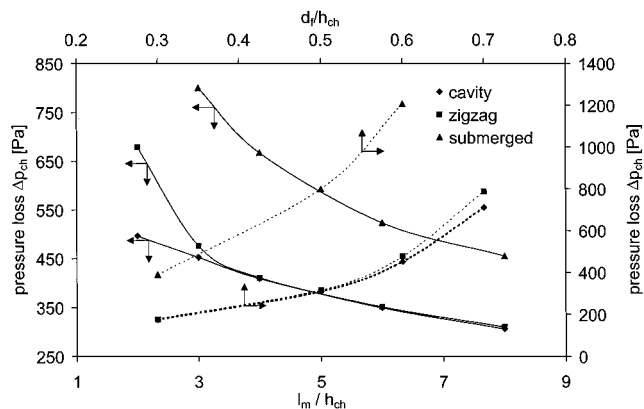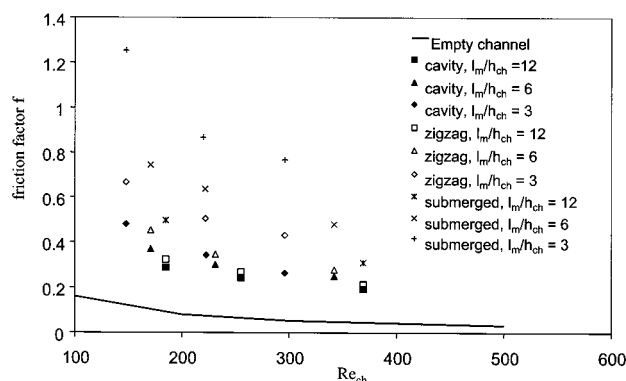

a

b

Figure 10. (a) Flow between sequential filaments for the submerged-type spacer for Re_{ch} from 90 to 400 and l_m/h_{ch} equal to 1.5 and 1 ($d_f/h_{ch} = 0.5$). (b) Shear stress distribution for the submerged spacer on the top wall between sequential filaments ($d_f/h_{ch} = 0.5$, $l_m/h_{ch} = 4$, and $Re_{ch} = 171$).

regions between sequential filaments at much smaller mesh lengths because the recirculation region behind a submerged filament is much smaller and thus has less impact on a downstream filament.

The characteristic shear stress distribution between sequential filaments for the submerged spacer shows that the maximum absolute wall shear stress is achieved at each wall immediately above and underneath each filament. The lowest absolute wall shear stress is achieved halfway between two sequential filaments on each wall, as shown in Figure 10b.

For the range of d_f/h_{ch} from 0.16 to 0.7 examined here, one large recirculation region between sequential filaments was formed when the characteristic mesh length to filament ratio l_m/d_f is decreased below 4 at $Re_{ch} = 171$. Above the characteristic value of l_m/d_f, the recirculation region behind each filament of a multiple-filament submerged spacer develops in a manner similar to that for a single submerged filament.

For both the cavity and submerged spacers, a small Re_{ch} or a large mesh length results in the formation of separate recirculation regions between sequential filaments. When Re_{ch} is increased at fixed mesh length or

Figure 12. Friction factor for the spacers at various mesh lengths ($d_f/h_{ch} = 0.5$) and the empty channel.

formation of the highly dissipative recirculation regions behind each filament.

7. Conclusions

The simulations showed complex relationships between the flow patterns, pressure loss, shear stress on the walls, filament configurations, mesh lengths, filament diameters, and Reynolds number in narrow and obstructed channels such as those found in spiral wound membrane modules. Recirculation regions are formed before and after each filament, with the size and shape of the regions being dependent on the spacer configuration, filament diameter, mesh length, and Reynolds number. Pressure loss increases with the Reynolds number and filament diameter and with a decrease in the mesh length and is also dependent on the spacer type. The submerged spacer shows a much higher wall shear stress but at a higher pressure loss than the cavity and zigzag spacers.

Although the calculations completed in this paper for the channel are in two dimensions, they are a fundamental step in being able to understand the fluid flow around spacer filaments obstructing a channel, before performing simulations in three dimensions. The results can be used to select appropriate conditions and parameters for three-dimensional calculations.

An effective spacer for a spiral wound module must provide a high mass-transfer rate from the membrane wall toward the bulk stream to reduce the wall concentration while maintaining a low pressure loss along the channel. From these hydrodynamic studies, it can be concluded that wall shear stress and the size of the recirculation regions, which changed with Reynolds number, filament diameter, and mesh length, will probably have a significant effect on the mass-transfer enhancement of a spacer-filled channel. A large mesh length allows redevelopment of the boundary layer between the filaments. Reducing the mesh length leads to a more frequent disturbance of the boundary layer. However, when the mesh length is small, the pressure loss becomes high and a large amount of membrane area is covered by adjacent spacer filaments and may become unavailable for permeation. A comprehensive analysis of the spacer performance, therefore, requires direct consideration of the effects of spacers on mass-transfer enhancement. This is the subject of a subsequent paper. With knowledge of the flow pattern, the pressure loss, and the mass-transfer characteristics of spacers, it should be possible to design improved spacers.

List of Symbols

C_{TD} = total drag coefficient
d_f, d_{f1}, d_{f2} = filament diameters, m
d_h = hydraulic diameter, m
f = friction factor
h_{ch} = channel height, m
l_m, l_{m1}, l_{m2} = mesh lengths, m
L = channel length, m
L_R = reattachment length, m
p = pressure, Pa
Δp_{ch} = pressure loss along the channel, Pa
Re_{ch} = Reynolds number of the spacer-filled channel
Re_{cyl} = cylinder Reynolds number
u_{ave} = average velocity in the channel
α = angle of the spacer filaments toward the flow, deg
β = constant in eq 6
γ = constant in eq 6
λ = constant in eq 6
μ = dynamic viscosity, Pa·s
ν = kinematic viscosity, m^2/s
θ = angle between the spacer filaments, deg
ρ = density, kg/m^3

Literature Cited

(1) Schlichting, H. *Boundary layer theory*; McGraw-Hill Book Co. Inc.: New York, 1960.
(2) DaCosta, A. R.; Fane, A. G.; Wiley, D. E. Ultrafiltration of whey protein solutions in spacer-filled channels. *J. Membr. Sci.* **1993**, *76*, 245.
(3) DaCosta, A. R.; Fane, A. G. Net-type spacers: Effect of configuration on fluid flow path and ultrafiltration flux. *Ind. Eng. Chem. Res.* **1994**, *33*, 1845.
(4) Da Costa, A. R.; Fane, A. G.; Fell, C. J. D.; Franken, A. C. M. Optimal channel spacer design for ultrafltration. *J. Membr. Sci.* **1991**, *62*, 275.
(5) Light, W. G.; Tran, T. V. Improvement of Thin-Channel Design for Pressure-Driven Membrane Systems. *Ind. Eng. Chem. Process Des. Dev.* **1981**, *20*, 33.
(6) Probstein, R. F.; Shen, J. S.; Leung, W. F. Ultrafiltration of Macromolecular Solutions at High Polarization in Laminar Channel Flow. *Desalination* **1978**, *24*, 1.
(7) Poyen, S.; Quemeneur, F.; Bariou, B.; Desille, M. Improvement of the flux of permeate in ultrafiltration by turbulence promoters. *Int. Chem. Eng. J.* **1987**, *27*, 441.
(8) Belfort, G.; Guter, G. An Experimental Study of Electrodialysis Hydrodynamics. *Desalination* **1972**, *10*, 221.
(9) Farkova, J. The pressure drop in membrane module with spacer. *J. Membr. Sci.* **1991**, *64*, 103.
(10) Schwinge, J.; Wiley, D. E.; Fane, A. G. Flux improvements with a new designed spacer geometry for ultrafiltration. Proceedings of the 6th World Congress of Chemical Engineering, Melbourne, Australia, Sept 2001.
(11) Kozlu, H.; Mikic, B. B.; Patera, A. T. Turbulent heat transfer augmentation using microscale disturbances inside the viscous sublayer. *J. Heat Transfer* **1992**, *114*, 348.
(12) Karniadakis, G. E.; Mikic, B. B.; Patera, A. T. Minimum-dissipation transport enhancement by flow destabilization: Reynolds' analogy revisited. *J. Fluid Mech.* **1988**, *192*, 365.
(13) Zdravkovich, M. M. Smoke observations of the formation of a Karman vortex street. *J. Fluid Mech.* **1969**, *37*, 491.
(14) Aref, H.; Siggia, E. D. Evaluation and breakdown of a vortex street in two dimensions. *J. Fluid Mech.* **1981**, *109*, 435.
(15) Eaton, B. E. Analysis of laminar vortex shedding behind a circular cylinder by computer-aided flow visualization. *J. Fluid Mech.* **1987**, *180*, 117.
(16) Perry, A. E.; Chong, M. S.; Lim, T. T. The vortex-shedding process behind two-dimensional bluff bodies. *J. Fluid Mech.* **1982**, *116*, 77.
(17) Greiner, M.; Chen, R. F.; Wirtz, R. A. Enhanced heat transfer/pressure drop measured from a flat surface in a grooved channel. *J. Heat Transfer* **1991**, *113*, 498.
(18) Greiner, M. An experimental investigation of resonant heat transfer enhancement in grooved channels. *Int. J. Heat Mass Transfer* **1991**, *34*, 1383.

(19) Greiner, M.; Chen, R. F.; Wirtz, R. A. Heat transfer augmentation through wall-shape-induced flow destabilization. *J. Heat Transfer* **1990**, *112*, 336.

(20) Majumdar, D.; Amon, C. H. Heat and momentum transport in self-sustained oscillatory viscous flow. *J. Heat Transfer* **1992**, *111*, 866.

(21) Amon, C. H.; Majumdar, D.; Herman, C. V.; Mayinger, F.; Mikic, B. B.; Sekulic, D. P. Numerical and experimental studies of self-sustained oscillatory flows in communicating channels. *Int. J. Heat Mass Transfer* **1992**, *35*, 3115.

(22) Thomas, D. G. Forced Convection Mass Transfer: Part II. Effect of Wires Located near the Edge of the Laminar Boundary Layer on the Rate of Forced Convection from a Flat Plate. *AIChE J.* **1965**, *11*, 848.

(23) Kim, D. H.; Kim, I. H.; Chang, H. N. Experimental Study of Mass Transfer around a Turbulence Promoter by the Limiting Current Method. *Int. J. Heat Mass Transfer* **1983**, *26*, 1007.

(24) Kang, I. S.; Chang, H. N. The Effect of Turbulence Promoters on Mass Transfer—Numerical Analysis and Flow Visualization. *Int. J. Heat Mass Transfer* **1982**, *25*, 1167.

(25) Cao, Z.; Wiley, D. E.; Fane, A. G. CFD simulation of net-type turbulence promoters in a narrow channel. *J. Membr. Sci.* **2001**, *185*, 157.

(26) Fox, R. W.; McDonald, A. T. *Introduction to Fluid Mechanics*; John Wiley & Sons: New York, 1994.

(27) *CFX 4.3 user manual*; CFX International, AEA Technology plc.: Harwell, Didcot, Oxfordshire, U.K., 2000.

(28) Schock, G.; Miquel, A. Mass transfer and pressure loss in spiral wound modules. *Desalination* **1987**, *64*, 339.

(29) Fletcher, D. F.; Maskell, S. J.; Patrick, M. A. Heat and mass transfer computations for laminar flow in axisymmetric sudden expansion. *Comput. Fluids* **1985**, *13*, 207.

(30) van Dyke, M. *An Album of Fluid Motion*; The Parabolic Press: Stanford, CA, 1982.